Determining interface structures in vertically aligned nanocomposite films [EP]

Bonan Zhu [iD], Georg Schusteritsch [iD], Ping Lu, Judith L. MacManus-Driscoll [iD], and Chris J. Pickard [iD]

COLLECTIONS

[EP] This paper was selected as an Editor's Pick

View Online   Export Citation   CrossMark

ARTICLES YOU MAY BE INTERESTED IN

Atomically interface engineered micrometer-thick $SrMoO_3$ oxide electrodes for thin-film $Ba_xSr_{1-x}TiO_3$ ferroelectric varactors tunable at low voltages
APL Materials 7, 051107 (2019); https://doi.org/10.1063/1.5094855

Large-area cost-effective lithography-free infrared metasurface absorbers for molecular detection
APL Materials 7, 071102 (2019); https://doi.org/10.1063/1.5102106

Barrier materials for flexible bioelectronic implants with chronic stability—Current approaches and future directions
APL Materials 7, 050902 (2019); https://doi.org/10.1063/1.5094415

ORDER PRINT EDITION

AIP Conference Proceedings
The 18th International Conference on Positron Annihilation

Determining interface structures in vertically aligned nanocomposite films

View Online   Export Citation   CrossMark

Bonan Zhu,[1,a] (iD) Georg Schusteritsch,[1,2] (iD) Ping Lu,[3] Judith L. MacManus-Driscoll,[1] (iD) and Chris J. Pickard[1,2] (iD)

AFFILIATIONS

[1] Department of Materials Science and Metallurgy, University of Cambridge, Cambridge, United Kingdom
[2] Advanced Institute for Materials Research, Tohoku University, 2-1-1 Katahira, Aoba, Sendai 980-8577, Japan
[3] Sandia National Laboratories, Albuquerque, New Mexico 87185, USA

[a] Electronic mail: bz240@cam.ac.uk

ABSTRACT

Vertically aligned nanocomposite (VAN) films have self-assembled pillar-matrix nanostructures. Owing to their large area-to-volume ratios, interfaces in VAN films are expected to play key roles in inducing functional properties, but our understanding is hindered by limited knowledge about their structures. Motivated by the lack of definitive explanation for the experimentally found enhanced ionic conductivity in Sm-doped-CeO_2/$SrTiO_3$ VAN films, we determine the structure at vertical interfaces using random structure searching and explore how it can affect ionic conduction. Interatomic potentials are used to perform the initial searching, followed by first-principles calculations for refinement. Previously unknown structures are found, with lower energy than that of an optimized hand-built model. We find a strongly distorted oxygen sublattice which gives a complex landscape of vacancy energies. The cation lattice remains similar to the bulk phase, but has a localized strain field. The excess energy of the interface is similar to that of high angle grain boundaries in $SrTiO_3$.

I. INTRODUCTION

Oxide thin films have a wide range of applications in electronic, magnetic, and energy devices. Vertically aligned nanocomposite (VAN) films[1–3] are a new form of thin film material which contain nanopillars of one phase embedded in a matrix of another. Because of unique strain states, uniform strain, large area of interfaces, and perfectly clean interfaces in these structures,[4–7] they have been attracting a lot of interest for a wide range of functional systems.[3,8] Also, VAN structures are easy to fabricate compared to planar superlattice films—they grow by self-assembly from a single target material using pulsed laser deposition, and the density of interfaces is very high with nanopillars of sizes around 10–20 nm.

It is widely known that interfaces strongly influence mechanical, electrical, and magnetic properties and also that at interfaces in planar heterostructures, novel functional properties often emerge.[9–11] The local environment at an interface can be very different from that of the bulk material, which leads to reconstruction of the atomic and electronic structures. In VANs, the pillar-matrix nanostructure results in a large and thickness independent interface-to-volume ratio. The two phases with different structures are tightly coupled though these vertical interfaces. While theoretical and computational approaches are invaluable for studying interfaces, the atomic configurations need to be known to start with. Experimental determination of interface structures is very challenging. Although the advancement in scanning transmission electron microscopy (STEM) has allowed individual atomic columns to be imaged, determining the local structures often still requires extensive simulations and sometimes intuition.

Recently, computational algorithms have been developed and enabled the prediction of structures for a range of materials.[12–15] *Ab initio* random structure searching (AIRSS) has been shown to successfully find stable structures for bulk crystals,[16–18] low dimensional structures,[19] point defects,[20,21] and interfaces.[22] Other search methods, such as those based on genetic algorithms and Bayesian optimizations, have also been reported to address structures at grain boundaries[23–26] and heterostructures.[27,28]

In this work, we study the interfaces in VAN films consisting of Sm-doped-CeO_2(20 at. %) pillars embedded in a matrix of $SrTiO_3$

(STO). Sm-doped-CeO$_2$ has a fluorite structure and is an ionic conductor,[29] while STO has a perovskite structure and is insulating. The former undergoes a 45° rotation when epitaxially grown on STO substrates such that its [110] direction is aligned with the [100] direction of STO. A schematic of the nanostructure and crystallographic directions is shown in Fig. 1(d). This system and similar ones have been reported to give enhanced ionic conductivity along the out-of-plane direction,[6,30,31] which makes them particularly attractive for micro solid oxide fuel cell applications. On the other hand, the roles of the vertical interfaces are still unclear. The effects of solid-solid interfaces on ionic conduction have been widely studied theoretically in planar heterostructures where the interface is between materials with the same structure[32,33] or its effect is dominated by the strain.[34,35] Only a few works directly addressed the interface structure.[27,28,36] We are not aware of any atomic scale computational studies about the vertical interfaces in VAN films, to date. The mismatch in periodicity and the fact that two sides have different bulk structures make these interfaces rather complex. While the high crystallinity of the films (i.e., low defect concentration) has been suggested to be the key to the enhanced ionic conduction,[30,31] the possibility that enhancements also occur along interfaces needs to be determined in a definitive way. Doing this experimentally is very difficult owing to the very small (sub-nanometer length scales) and low volumes of the material involved in thin films and so theoretical approaches are very important to guide the understanding.

Using STEM images as the starting point, we determine the interface atomic configurations using random structure searching. A combination of interatomic potential and first-principles methods is used, which will be described in Sec. II. We found previously unknown interface structures with lower energies than those of a locally optimized hand-built model. These structures share common motifs and have a highly distorted anion lattice. The implications of the findings in the context of local ionic conduction enhancement are discussed.

II. METHODS

A. Simulation details

We choose to focus on the interfaces formed between (100) and (110) planes of SrTiO$_3$ (STO) and Sm-doped-CeO$_2$ (SDC) as electron microscopy images show that the majority of them are in this orientation. They are indicated with blue lines in Fig. 1(b). The image is captured with a scanning transmission electron microscope in high angle annular dark field mode. The minor STO(110)/SDC(100) type interfaces are marked by green lines. The orientation, periodicity, and alignment of atomic planes of the vertical interface can be inferred from the cross-sectional STEM image shown in Fig. 1(a). It appears that 7 unit cells of STO match to 5 unit cells of SDC in the [001] direction, as indicated by the arrows. Figure 1(c) shows matching of atomic planes at the vertical interface viewed along the [001] direction. We construct a schematic
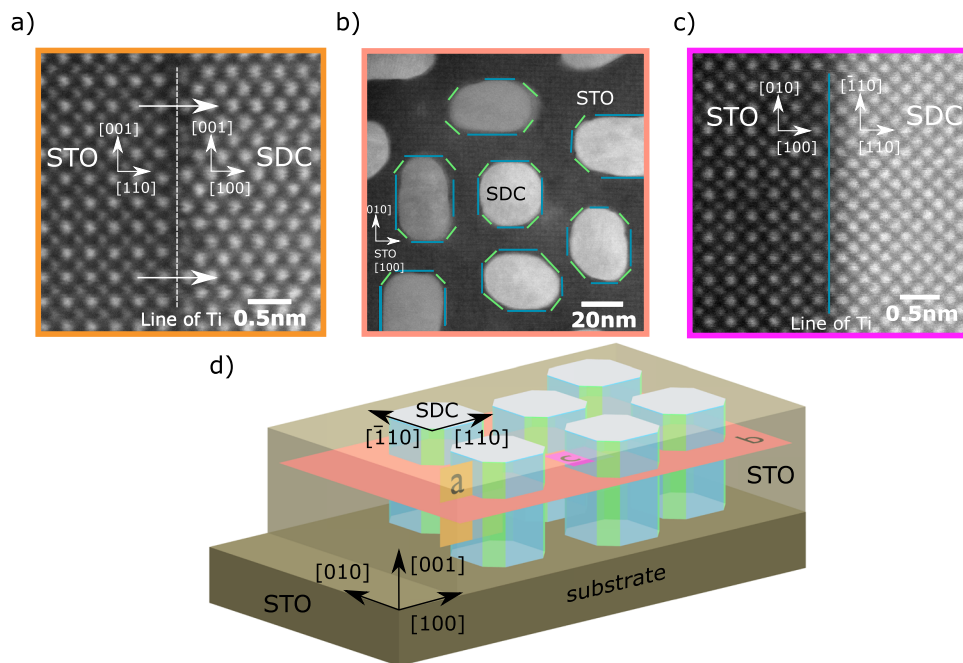

FIG. 1. (a) A cross-sectional STEM high-angle annular dark-field (HAADF) image showing the STO(100)-SDC(110) interface viewed in the STO[010] direction. The two horizontal arrows mark the periodicity in the [001] direction. The vertical dashed line indicates the TiO$_2$ (100) termination plane of STO. (b) A plane view STEM HAADF image showing bright SDC columns embedded in a darker STO matrix. The STO(100)-SDC(110) interface studied in this work is marked by the blue lines. The green lines mark the minor STO(110)-SDC(100) interfaces. (c) A high magnification STEM HAADF image showing the STO-SDC vertical interface viewed along the [001] direction. The blue line marks the interface. (d) A schematic of the VAN film structure. The SDC pillars are embedded in a matrix of STO with specific crystallographic matching. The image planes of (a)–(c) are labeled.

of the pillar-matrix nanostructure [shown in Fig. 1(d)] based on the images. Crystallographic directions and imaging planes of Figs. 1(a)–1(c) are labeled. Note that the STO matrix has the same orientation as the substrate.

As the starting point for structure searching, we construct an idealized interface model by joining the bulk structures. We limit ourselves to TiO$_2$ terminated STO as a faint line of Ti atoms can be identified between the two lattices, shown in Fig. 1(a) with a dotted vertical line. The orientation relationship of the two sides is set to be consistent with plane view and cross-sectional STEM images as in Figs. 1(a) and 1(c). The experimental lattice constant of STO is 3.905 Å and that of CeO$_2$ is 5.41 Å. In the [001] direction, we match seven unit cells of STO to five unit cells of CeO$_2$. Two unit cells of STO along its [010] direction are included with matching units of CeO$_2$. We use the experimental lattice constant for STO and adjust that of CeO$_2$ to match in the interface plane. This means that CeO$_2$ is compressively strained by 2.0% along the STO[010] direction and tensile strained by 1.0% along the STO/CeO$_2$[001] direction. We do not expect the strain to significantly affect the interface structures. As a first approximation, we neglect the Sm dopants (20 at. %) in the structure searching, and hence, the problem becomes finding the stable interface structure between STO (100) and CeO$_2$ (110). Including dopants would significantly increase the search space of the interface structures. The cubic $Fm\bar{3}m$ phase of CeO$_2$ is stable at low-temperatures in contrast to yttria-stabilized zirconia (YSZ) where the yttria dopant plays an important role in stabilizing the cubic phase.

Interfaces are inherently nonperiodic along its normal direction. There are two schemes for embedding an interface in a periodic cell. A single interface can be formed by two slabs of the material, and this composite slab is then separated from its periodic images by vacuum. To mimic bulk boundary conditions, we add extra bulk layers to the exposed surfaces. These layers are internally fixed but allowed to move as a whole. An alternative scheme is to construct a cell with two identical interfaces which are mirror images of each other. This is only possible because the bulk phases both have mirror planes parallel to the interface. Exposed surfaces are avoided at the price of almost doubling the number of atoms. Illustrations of the two schemes are found in the supplementary material.

In-depth discussion of AIRSS[37] and how it can be applied to interface structure prediction have been described in a previous work.[22] Here, we outline only the most relevant details in this study. AIRSS relies on generating random but physically sensible structures which are subsequently relaxed. To limit the search space, we choose species-pair dependent minimum atomic separation constraints based on the values in bulk STO and CeO$_2$. We also choose the randomized region to be within 1 or 2 atomic layers from the interface, which will be discussed later. Instead of full randomization, we displace atoms randomly from their positions in the idealized model. This avoids forming clusters of similarly charged ions, which otherwise can give rise to high electrostatic energies. Maximum displacement magnitudes of 4 Å and 2 Å are used in lateral and normal directions to the interface, respectively. Random structures generated with these parameters no longer have the pre-existing order at the interface as in the initial model. Periodic cells with two identical interfaces are used for searching using interatomic potentials. Selected low energy structures are converted into slab models that each includes a single interface for further density

functional theory (DFT) calculations. More details are found in the supplementary material.

DFT calculations are exceedingly expensive to use for structure searching of systems that contain as many atoms as the interfaces require here, since even a minimal cell in the slab geometry including 4 atomic layers for each side already has 260 atoms. Hence, we choose to use empirical interatomic potentials for searching, followed by refinement DFT calculations. Buckingham potentials with long-range Coulomb interactions are used. For STO, we apply the same potentials which were used in previous structure searching works of STO grain boundaries[23] and ZrO$_2$-STO superlattices.[27,28] The potentials chosen for CeO$_2$ were previously used for studying dopant distribution and ionic transport near edge dislocations.[38] Details of the potentials are found in the supplementary material.[39] The General Utility Lattice Program[39] (GULP) is used for relaxing random structures. The dual interface scheme described above is used. The cell size normal to the interface is allowed to relax.

Density functional theory calculations are performed using the plane-wave pseudopotential code CASTEP.[40] Generalized gradient approximation based exchange-correlation functionals have been used in many other computational studies of STO and CeO$_2$ and were shown to give consistent results.[32,41–44] PBEsol[45] is used here since it gives lattice constants closer to the experimental values for both STO and CeO$_2$. The valence states $2s^2\ 2p^4$ for O, the $3s^2\ 2p^6\ 3d^2\ 4s^2$ states for Ti, the $4s^2\ 4p^6\ 5s^2$ states for Sr, and the $4f^1\ 5s^2\ 5p^6\ 5d^1\ 6s^2$ states for Ce are treated using on-the-fly generated core-corrected ultrasoft pseudopotentials. These pseudopotentials are soft and allow a plane wave cutoff energy of 350 eV to be used. Their generation settings are tabulated in the supplementary material. A Monkhorst-Pack grid of $1 \times 4 \times 1$ is used for sampling the Brillouin zone. We used the slab scheme described above to embed the interface in a periodic cell. The lattice constants are fixed during the geometry optimization.

The Atomic Simulation Environment[46] (ASE) is used for setting up and manipulating structures. AiiDA[47] is used to prepare, submit, and parse results for DFT calculations. To distinguish and classify the structures found, Smooth Overlap of Atomic Positions[48] (SOAP) implemented in the GAP suite[49] is used. More details are included in the supplementary material.

B. Experimental details

The Sm-doped-CeO$_2$/SrTiO$_3$ vertically aligned nanocomposite (VAN) film was prepared by pulsed-laser deposition (PLD) as described previously.[50] An FEI TitanTM G2 80-200 scanning transmission electron microscope with a Cs probe corrector operated at 200 kV was used in this study. The STO/SDC interfaces were imaged by using a high-angle annular dark-field (HAADF) detector with a collection range of 60–160 mrad.

III. RESULTS AND DISCUSSION

We first check the effectiveness of our RSS approach by searching for the bulk structures of SrTiO$_3$ (STO) and CeO$_2$ using both DFT and interatomic potentials. An $I4/mcm$ phase of STO is found to have the lowest energy using DFT for relaxation which is consistent with the low temperature phase of STO found experimentally.[51] Using the interatomic potentials, the $Pm\bar{3}m$ cubic structure is found

as the most stable one. The $Pm\bar{3}m$ phase is the high temperature phase and was found in the VAN films previously.[30,50] For CeO$_2$, the $Fm\bar{3}m$ fluorite structure is the most stable one using both methods. These findings are consistent with experimental results[51–53] and existing structural prediction works.[22,23,27,28]

Due to the large quantity of relaxed random structures, we choose to focus on structures that have low relative energies and can be found repetitively. The relative energy for each structure is defined as

$$E_{rel} = E_{total} - E_{total}^{ref}, \tag{1}$$

where E_{total} is the total energy and E_{total}^{ref} is the total energy of the reference structure which is chosen to be the structure with the lowest total energy. We note that the interatomic potentials can give additional local minima in its potential energy surface (PES) compared to DFT due to their fixed analytic form. Assuming a uniform sampling of the configuration space, the number of visits to the same minima is proportional to the hypervolume of the basin it is in. These frequently visited minima are likely to represent basins that also exist in the real PES.

To check if the randomization zone is sufficiently large, we perform searches with one or two randomized atomic layers in each side of the interface. Having one extra layer shifts the distribution of the relative energies toward higher values with a broader spread. Most of the low energy structures can be found in both searches. Since none of the low energy structures is exclusively found with increased randomization zone size, we limit the number of randomized layers to be one on both sides in subsequent searches.

Due to the finite size of the search cells, interactions between an interface and its mirror images can affect the geometry optimized structures as well as their relative energies. To check the convergence of structures with respect to the number of layers included normal to the interface, we carry out searches with 4–10 layers. While up to 10 layers were required to converge relative energies between the unique structures, most of the structures can be found even with the lowest setting of 4 layers. This indicates that interface self-interactions have a limited effect on

the overall shape of the PES, despite the values of minima being shifted.

The five low energy structures found in this work are shown in Fig. 2. The two lowest energy structures A and B are different in oxygen positions in the last SrO layer, and each has a glide plane with space group Pc. A highly symmetric structure C^* is also found. It has a space group $Pmm2$ and is 1.1 eV higher in energy in searches including 6 layers of material on each side. In fact, this structure can be obtained by a simple local optimization of the initial model structure. Two other structures D and E both lack any symmetry element. A common pattern emerges among these five structures as well as in many others that have low relative energies. In Fig. 2, we fade out the regions where the atomic configurations are shared by different structures. This highlights where they differ from each other which is also where the oxygen sublattice is very different from the bulk phases.

Details of structure A are shown in Fig. 3. The bulk structures of STO and CeO$_2$ are vastly different. In perovskite-structured STO, Ti atoms are six-fold coordinated by oxygen atoms in a vertex-sharing octahedron network. The Sr atoms are twelve-fold cuboctahedron coordinated, and each cuboctahedron shares faces with the adjacent ones. In fluorite structured CeO$_2$, Ce atoms are coordinated by eight oxygen atoms and coordination cubes share their edges. At the interface where 7 units cells of STO match to 5 unit cells of CeO$_2$, the stacking sequence of STO (001) planes (i.e., SrO-TiO$_2$-SrO-TiO$_2$) and CeO$_2$ (110) planes (i.e., CeO$_2$-CeO$_2$) ends abruptly. If the sequences were not disrupted, 7 oxygen atoms would be placed in the next layer of the terminal TiO$_2$ plane, which continues the vertex-sharing Ti-O octahedron network. In reality, there are 10 oxygen atoms in the adjacent CeO$_2$(001) plane. Similarly, it would have been 10 oxygen atoms in the next layer of the terminal CeO$_2$ plane, but only 7 adjacent oxygen atoms are present in the TiO$_2$ layer of STO [Fig. 3(b)]. Hence, the Ti atoms at the interface are over-coordinated and Ce atoms are under-coordinated. The latter is shown by the missing vertices of the Ce-O cube at the interface in Fig. 3(c). The mismatch of the bulk structure at the interface is mostly accommodated via the rearrangement of the oxygen sublattice, as highlighted by the rectangles in Figs. 3(a) and 3(b). On the
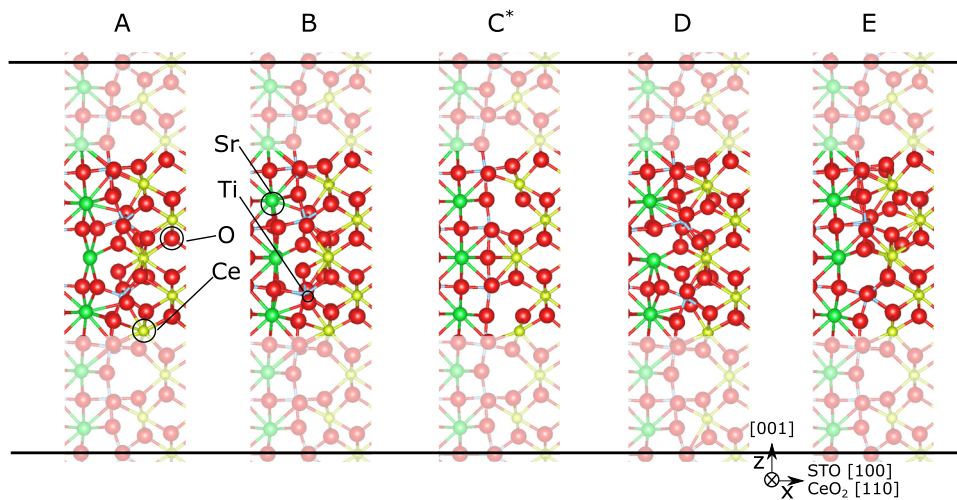

FIG. 2. Low energy structures found using the interatomic potentials, looking down the y (STO[010]) direction to show the atomic arrangements along z (STO[001]). We include only a small section of each simulation cell along x (STO[100]) to focus on the atomic configuration at the interfaces. The regions where atomic arrangement is shared are faded out in order to highlight the differences between these structures. Note that structure C^* is the result of a simple local optimization of the idealized model and is also found during the search.
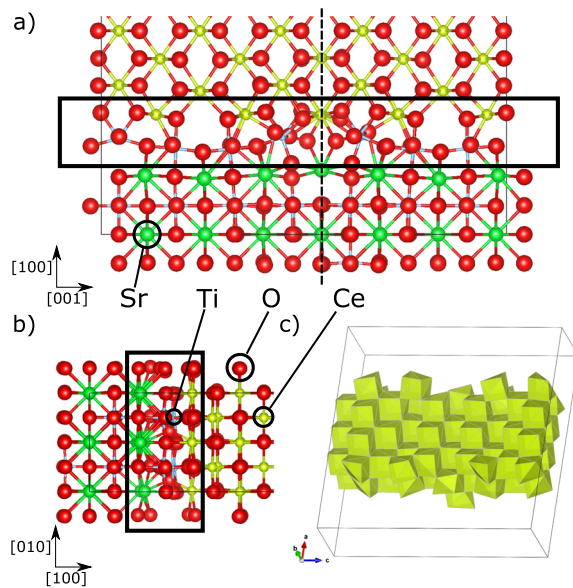
FIG. 3. Illustrations of structure A that has the space group Pc. (a) Viewing along the STO[010] direction. The glide plane is indicated by the dashed line. (b) Viewing along the [001] direction. (c) Distorted Ce-O$_8$ coordination polyhedron at the interface. Some of them have corners missing. Distortions of the Ti-O$_6$ octahedra are highlighted with rectangles in (a) and (b).

FIG. 4. Comparing the energy difference per unit area given by DFT (σ_{dft}^{rel}) and interatomic potentials (σ_p^{rel}). Structures are labeled by their name and symmetry. A positive correlation can be seen over the plotting range, indicated by the blue fitted line. On the other hand, there is little correlation when focused on the details over a small range, as shown in the inset.

other hand, there is little distortion in the cation lattice at the interface, which is consistent with the STEM images [shown in Figs. 1(a)–1(c)], where visually there is little change in the atomic arrangement at the interfaces compared to the bulk. Note that the complex distortion of the anion lattice is missing in these images due to the relatively low atomic number of O atoms. This highlights the power of performing structure searching to reveal the full lattice information. The optimized initial model (structure C^*) has the space group $Pmm2$. Most of the structures found do not have any symmetry present at all, apart from a few at the low energy end of the distribution. Structure A has a glide plane parallel to the (001) planes with a translation of half of the lattice vector in the STO[010] direction. This is marked by the dotted line in Fig. 3(a).

We next carry out DFT calculations on nine candidate structures and compare their relative energies with those given by the interatomic potentials. Our checks are limited to structures with six layers of materials on each side, due to the increasing computational costs with the cell size. In Fig. 4, the energy differences per unit interface area ($\sigma^{rel} = E_{rel}/A_{itf}$) from DFT and interatomic potential calculations are plotted for comparison. In addition to the low energy structures, we include six structures with higher energy and label them as S1-6. A line is fitted to the data showing a positive correlation between the energies given by the two levels of theory over the plotting range. However, we find no correlation among the closely spaced low energy structures themselves, as shown in the inset of Fig. 4. Structure E turns out to have the lowest energy given by DFT calculations, while it is 7 meV Å^{-2} higher in energy given by the interatomic potentials. In addition, A and B are two distinct structures found with the interatomic potentials, but they become
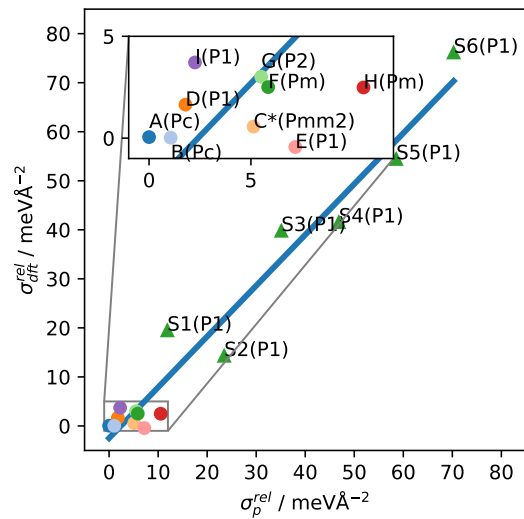
the same after being optimized with DFT. It is known that empirical interatomic potentials can give more local minima. Ideally, we would like to search directly with DFT, but for a system as large as we consider here, it is prohibitively expensive to do so. The details of the PES are certainly different between these two levels of theory. Nevertheless, the trend over a relatively large energy range ($\approx$70 meV Å^{-2}) is still captured by the interatomic potentials. The absence of correlations over a small energy range ($\approx$10 meV Å^{-2}) means that it is necessary to refine a collection of structures with DFT calculations.

We compute the local strain for Ce atoms based on the averaged nearest neighbor distances normalized by the mean value. The same is also done for STO using the Ti-Ti distances. In Fig. 5(b), each square represents a Ce column in structure E and each triangle represents a Ti column, looking down the STO[010] direction. The sign of the strain alternates on each side of the interface going along the [001] direction. Tensile strained regions in CeO$_2$ are adjacent to compressively strained regions in STO. This strain field is quickly suppressed going into the bulk. Similar patterns also exist in other structures.

The interface can also influence the defect energy of oxygen vacancies. We calculate relative defect energies of oxygen vacancies in these structures using the interatomic potentials. A map of the relative formation energies in structure E is shown in Fig. 5(a). Here, oxygen sites are marked with circles, and the defect energy of bulk CeO$_2$ is chosen as the reference. All four atomic layers parallel to (010) planes of STO are included. The sizes of the circles are set according to their distances in the [010] direction such that those further away appear smaller and may be overlapped by those in the front. A few sites at the interface have lower defect energy compared to that of the bulk, indicated by the dark green region in Fig. 5(a).
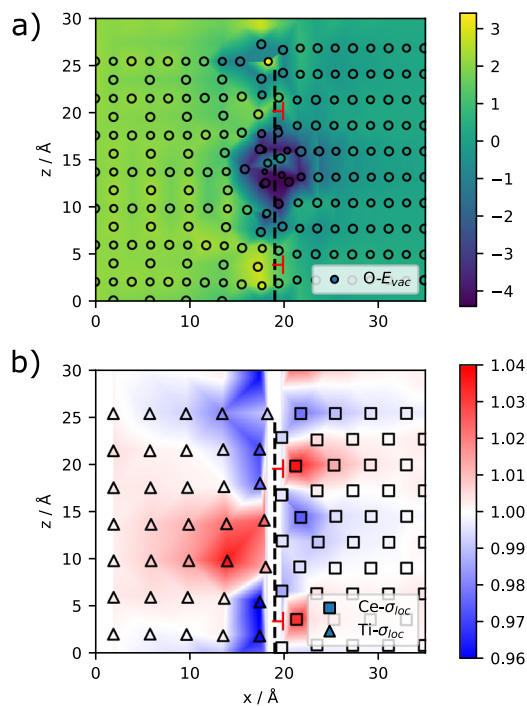
FIG. 5. (a) Relative defect energies of oxygen vacancies mapped in the x-z plane for structure E, viewed in the same direction as that of Fig. 2. The circles represent oxygen positions. The reference is set to the oxygen vacancy energy of bulk CeO_2. (b) Local strain of the Ce lattice in CeO_2 for the same view. Ce and Ti are labeled with squares and triangles, respectively. The vacancy energy is related to the degree of distortion from the bulk lattice but not to the strain field. The two misfit dislocations are also marked in red at the interface.

We note that the existence of sites with very low defect energy suggests that nonstoichiometric structures can become stable. However, it is challenging to perform the search with nonstoichiometric compositions since the interatomic potentials assume fixed ionic charges. The key point is that the mismatch in the crystal structure results in a complex energy landscape of the oxygen vacancies at the interface, which is likely to cause substantial trapping during vacancy migration.

We calculate the excess energy of the vertical interface using the approach of previous studies.[54,55] More details can be found in the supplementary material. An excess energy of 0.91 J/m² is found for structure E. Note that the excess energies for STO symmetrical grain boundaries vary in a range of 0.5–1.5 J/m² depending on termination and orientation.[22–24] Despite significant structural mismatch, the vertical interface is energetically similar to the grain boundaries. The variation of excess energies among the low energy structures is on the order of 3 meV/Å² (0.05 J/m²). The small differences mean multiple configurations are accessible at elevated temperatures, resulting in a disordered anion lattice.

Misfit dislocations are important for heterogeneous interfaces in thin films as they allow the interface strain caused by the mismatch in the lattice constants to be relaxed. In the lattice match epitaxial growth model, the growth starts with one-to-one lattice mismatching, followed by dislocation formation at the film surface.

The dislocations then glide down to the film-substrate interface. An extension of this model is domain matching epitaxy (DME) which applies when the mismatch in the lattice parameter is so large that m lattice planes of one side are matched to n lattice planes of the other from the beginning of the growth,[56] where both m and n are integers. In this work, 7 STO lattice planes match to 5 CeO_2 lattice planes along the [001] direction. This can be regarded as alternating 3/2 and 4/3 matches between the two sides, which is consistent with the DME model. We identify two misfit dislocations at the vertical interface and indicate them in Fig. 5. They are consistent with the localized strain field, where CeO_2 is tensile strained and STO is compressively strained in the vicinity of each. However, the strongest distortion of the oxygen sublattice does not take place at the cores of dislocations, but is instead located in between them. In addition, the reduction of vacancy energy can be associated with the distortion of the anion lattice, as shown in Fig. 5(a), rather than located at the dislocation cores as reported in other studies.[38,57] One possible cause of this is that the dislocations are closely spaced (16 Å). The strongly distorted anion lattice, as we have here, is not predicted under the framework of misfit dislocations based on lattice geometry. This highlights the advantage of doing systematic structure searching for understanding heterogeneous interfaces.

We now discuss the implications of the structures we found on the ionic conductivity at the vertical interfaces. First, we found a strain field highly localized at the interface, as shown in Fig. 5. The effect of strain in fluorite structured ionic conductors has been studied in previous experimental and theoretical works.[31,34,35,58–60] The ionic conductivity is expected to increase when the lattice is subject to tensile strain due to the decrease in the migration barrier. However, these results apply to uniform or gradually decaying strain field. The situation is different here as the strain field is localized and microscopic. Furthermore, Sun et al. showed, through molecular dynamics, that the strain field caused by dislocations leads to segregation of the dopant ions in doped ceria.[38] Dopant ions often have different ionic radii compared to the Ce^{4+} ions, and by having them in the sites under local strain, the elastic energy could be reduced. Both local enrichment and depletion of dopants are detrimental to the ionic conduction. The former increases the migration barrier as a result of stronger dopant-vacancy interactions, while the latter reduces the concentration of vacancies.

Second, by calculating the oxygen vacancy defect energies, sites with low relative defect energies are found at the interfaces. Once a vacancy diffuses into one of these sites, it is less likely to move out as the energy barrier of migration becomes much higher. As a result, the ionic conductivity is reduced locally. This is consistent with the work of Dholabhai et al.,[57] where the diffusivity at the STO-MgO interface was calculated using the kinetic Monte Carlo method. It was found that vacancy mobility was lowered due to trapping sites originating from the network of misfit dislocations at the interface.

Third, the DFT energies of the low-energy structures are found to be very closely spaced. This indicates that the interface is less likely to take a single structure under a finite temperature. Such structural degeneracy mostly takes place in the anion lattice. While a disordered anion sublattice could lead to an enhancement in ionic conductivity,[61] we note that for the vertical interface this only takes place at the first interface layers of both sides. In addition, these disordered regions are confined, since they are separated by regions

where atomic configurations are shared in many candidate structures, as illustrated in Fig. 2. Hence, we do not expect that this alone can enhance the ionic conductivity in the [001] direction.

In summary, we found a collection of lower energy structures of the STO(100)-CeO$_2$(110) vertical interfaces, including those with lower energies than those of the optimized hand-built model (C*, Fig. 2). A highly distorted anion lattice was determined at these interfaces arising from the structural mismatch. The excess energies of interfaces are of the same order of magnitude as high angle grain boundaries in STO. We found that interface misfit dislocation models are insufficient to describe the complex landscape of vacancy defect energies and the localized strain field in the structures.

IV. CONCLUSIONS

Random structure searching is used to determine interface configurations of the SrTiO$_3$(100)-CeO$_2$(110) vertical interface which forms naturally in vertically aligned nanocomposite (VAN) thin films. Lattice information in STEM images is used to constraint the search space to interface terminations and orientations that are physically present. We find previously unknown structures with energies lower than those of a locally relaxed model built by hand (C*, Fig. 2). The interface excess energies of these structures are similar to those of high angle grain boundaries. We find highly distorted oxygen anion lattices at the interfaces, while the cation lattice mostly remains similar to that of the bulk phases. The complex landscape of the defect energies is consistent with oxygen vacancies being trapped at the interface, rather than their mobility being enhanced. For the cation lattice, we find that the strain field is nonuniform and is localized at the interface. Our findings provide a solid basis for further investigations on defect chemistry and migration of oxygen vacancies at the interface to reveal its effects on ionic conductivity. The structure searching approach can also be applied to other VAN systems showing a wide range of novel functionalities where the roles of vertical interfaces are not yet well understood.

SUPPLEMENTARY MATERIAL

See supplementary material for more details of the interatomic potentials, the pseudopotentials, interface structure searching, and computing the excess energy.

ACKNOWLEDGMENTS

REFERENCES

[1] J. L. MacManus-Driscoll, "Self-assembled heteroepitaxial oxide nanocomposite thin film structures: Designing interface-induced functionality in electronic materials," Adv. Funct. Mater. **20**, 2035–2045 (2010).

[2] J. L. MacManus-Driscoll, A. Suwardi, and H. Wang, "Composite epitaxial thin films: A new platform for tuning, probing, and exploiting mesoscale oxides," MRS Bull. **40**, 933–942 (2015).

[3] J. Huang, J. L. MacManus-Driscoll, and H. Wang, "New epitaxy paradigm in epitaxial self-assembled oxide vertically aligned nanocomposite thin films," J. Mater. Res. **32**, 4054–4066 (2017).

[4] J. L. MacManus-Driscoll, P. Zerrer, H. Wang, H. Yang, J. Yoon, A. Fouchet, R. Yu, M. G. Blamire, and Q. Jia, "Strain control and spontaneous phase ordering in vertical nanocomposite heteroepitaxial thin films," Nat. Mater. **7**, 314–320 (2008).

[5] A. Chen, J.-M. Hu, P. Lu, T. Yang, W. Zhang, L. Li, T. Ahmed, E. Enriquez, M. Weigand, Q. Su, H. Wang, J.-X. Zhu, J. L. MacManus-Driscoll, L.-Q. Chen, D. Yarotski, and Q. Jia, "Role of scaffold network in controlling strain and functionalities of nanocomposite films," Sci. Adv. **2**, e1600245 (2016).

[6] S. Lee, W. Zhang, F. Khatkhatay, Q. Jia, H. Wang, and J. L. MacManus-Driscoll, "Strain tuning and strong enhancement of ionic conductivity in SrZrO$_3$-RE$_2$O$_3$ (RE = Sm, Eu, Gd, Dy, and Er) nanocomposite films," Adv. Funct. Mater. **25**, 4328–4333 (2015).

[7] Q. Zhan, R. Yu, S. P. Crane, H. Zheng, C. Kisielowski, and R. Ramesh, "Structure and interface chemistry of perovskite-spinel nanocomposite thin films," Appl. Phys. Lett. **89**, 172902 (2006).

[8] W. Zhang, R. Ramesh, J. L. MacManus-Driscoll, and H. Wang, "Multifunctional, self-assembled oxide nanocomposite thin films and devices," MRS Bull. **40**, 736–745 (2015).

[9] A. Ohtomo and H. Y. Hwang, "A high-mobility electron gas at the LaAlO$_3$/SrTiO$_3$ heterointerface," Nature **427**, 423–426 (2004).

[10] S. Okamoto and A. J. Millis, "Electronic reconstruction at an interface between a Mott insulator and a band insulator," Nature **428**, 630–633 (2004).

[11] P. Yu, J.-S. Lee, S. Okamoto, M. D. Rossell, M. Huijben, C.-H. Yang, Q. He, J. X. Zhang, S. Y. Yang, M. J. Lee, Q. M. Ramasse, R. Erni, Y.-H. Chu, D. A. Arena, C.-C. Kao, L. W. Martin, and R. Ramesh, "Interface ferromagnetism and orbital reconstruction in BiFeO$_3$-La$_{0.7}$Sr$_{0.3}$MnO$_3$ heterostructures," Phys. Rev. Lett. **105**, 027201 (2010).

[12] C. J. Pickard and R. J. Needs, "High-pressure phases of silane," Phys. Rev. Lett. **97**, 045504 (2006).

[13] Y. Wang, J. Lv, L. Zhu, and Y. Ma, "Crystal structure prediction via particle-swarm optimization," Phys. Rev. B **82**, 094116 (2010).

[14] S. Goedecker, "Minima hopping: An efficient search method for the global minimum of the potential energy surface of complex molecular systems," J. Chem. Phys. **120**, 9911–9917 (2004).

[15] A. R. Oganov, C. W. Glass, and S. Ono, "High-pressure phases of CaCO$_3$: Crystal structure prediction and experiment," Earth Planet. Sci. Lett. **241**, 95–103 (2006).

[16] C. J. Pickard and R. J. Needs, "Structure of phase III of solid hydrogen," Nat. Phys. **3**, 473–476 (2007).

[17] C. J. Pickard and R. J. Needs, "When is H$_2$O not water?," J. Chem. Phys. **127**, 244503 (2007).

[18] G. Schusteritsch, S. P. Hepplestone, and C. J. Pickard, "First-principles structure determination of interface materials: The Ni$_x$InAs nickelides," Phys. Rev. B **92**, 054105 (2015).

[19] J. Chen, G. Schusteritsch, C. J. Pickard, C. G. Salzmann, and A. Michaelides, "Two dimensional ice from first principles: Structures and phase transitions," Phys. Rev. Lett. **116**, 025501 (2016).

[20] A. J. Morris, C. J. Pickard, and R. J. Needs, "Hydrogen/silicon complexes in silicon from computational searches," Phys. Rev. B **78**, 184102 (2008).

[21] A. J. Morris, C. J. Pickard, and R. J. Needs, "Hydrogen/nitrogen/oxygen defect complexes in silicon from computational searches," Phys. Rev. B **80**, 144112 (2009).

[22] G. Schusteritsch and C. J. Pickard, "Predicting interface structures: From SrTiO₃ to graphene," Phys. Rev. B **90**, 035424 (2014).

[23] A. L.-S. Chua, N. A. Benedek, L. Chen, M. W. Finnis, and A. P. Sutton, "A genetic algorithm for predicting the structures of interfaces in multicomponent systems," Nat. Mater. **9**, 418–422 (2010).

[24] X. Zhao, Q. Shu, M. C. Nguyen, Y. Wang, M. Ji, H. Xiang, K.-M. Ho, X. Gong, and C.-Z. Wang, "Interface structure prediction from first-principles," J. Phys. Chem. C **118**, 9524–9530 (2014).

[25] Q. Zhu, A. Samanta, B. Li, R. E. Rudd, and T. Frolov, "Predicting phase behavior of grain boundaries with evolutionary search and machine learning," Nat. Commun. **9**, 467 (2018).

[26] S. Kikuchi, H. Oda, S. Kiyohara, and T. Mizoguchi, "Bayesian optimization for efficient determination of metal oxide grain boundary structures," Physica B **532**, 24–28 (2018).

[27] W. L. Cheah and M. W. Finnis, "Structure of multilayer ZrO₂/SrTiO₃," J. Mater. Sci. **47**, 1631–1640 (2012).

[28] W. L. Cheah, D. W. McComb, and M. W. Finnis, "Structure and ionic diffusivity in an yttria-stabilised zirconia/strontium titanate multilayer," Acta Mater. **129**, 388–397 (2017).

[29] H. Yahiro, Y. Eguchi, K. Eguchi, and H. Arai, "Oxygen ion conductivity of the ceria-samarium oxide system with fluorite structure," J. Appl. Electrochem. **18**, 527–531 (1988).

[30] S. M. Yang, S. Lee, J. Jian, W. Zhang, P. Lu, Q. Jia, H. Wang, T. W. Noh, S. V. Kalinin, and J. L. MacManus-Driscoll, "Strongly enhanced oxygen ion transport through samarium-doped CeO₂ nanopillars in nanocomposite films," Nat. Commun. **6**, 8588 (2015).

[31] S. Lee, W. Zhang, F. Khatkhatay, H. Wang, Q. Jia, and J. L. MacManus-Driscoll, "Ionic conductivity increased by two orders of magnitude in micrometer-thick vertical yttria-stabilized ZrO₂ nanocomposite films," Nano Lett. **15**, 7362–7369 (2015).

[32] D. S. Aidhy, B. Liu, Y. Zhang, and W. J. Weber, "Strain-induced phase and oxygen-vacancy stability in ionic interfaces from first-principles calculations," J. Phys. Chem. C **118**, 30139–30144 (2014).

[33] D. S. Aidhy, Y. Zhang, and W. J. Weber, "Strained ionic interfaces: Effect on oxygen diffusivity from atomistic simulations," J. Phys. Chem. C **118**, 4207–4212 (2014).

[34] R. A. D. Souza, A. Ramadan, and S. Hörner, "Modifying the barriers for oxygen-vacancy migration in fluorite-structured CeO₂ electrolytes through strain: A computer simulation study," Energy Environ. Sci. **5**, 5445–5453 (2012).

[35] A. Kushima and B. Yildiz, "Oxygen ion diffusivity in strained yttria stabilized zirconia: Where is the fastest strain?," J. Mater. Chem. **20**, 4809 (2010).

[36] M. S. Dyer, G. R. Darling, J. B. Claridge, and M. J. Rosseinsky, "Chemical bonding and atomic structure in Y₂O₃:ZrO₂-SrTiO₃ layered heterostructures," Angew. Chem., Int. Ed. **51**, 3418–3422 (2012).

[37] C. J. Pickard and R. J. Needs, "*Ab initio* random structure searching," J. Phys.: Condens. Matter **23**, 053201 (2011).

[38] L. Sun, D. Marrocchelli, and B. Yildiz, "Edge dislocation slows down oxide ion diffusion in doped CeO₂ by segregation of charged defects," Nat. Commun. **6**, 6294 (2015).

[39] J. D. Gale and A. L. Rohl, "The general utility lattice program (GULP)," Mol. Simul. **29**, 291–341 (2003).

[40] S. J. Clark, M. D. Segall, C. J. Pickard, P. J. Hasnip, M. I. J. Probert, K. Refson, and M. C. Payne, "First principles methods using CASTEP," Z. Kristallogr.–Cryst. Mater. **220**, 567–570 (2005).

[41] Y. Choi, M. Scott, T. Söhnel, and H. Idriss, "A DFT+U computational study on stoichiometric and oxygen deficient M–CeO₂ systems (M = Pd1, Rh1, Rh10, Pd10 and Rh4Pd6)," Phys. Chem. Chem. Phys. **16**, 22588–22599 (2014).

[42] C. W. M. Castleton, J. Kullgren, and K. Hermansson, "Tuning LDA+U for electron localization and structure at oxygen vacancies in ceria," J. Chem. Phys. **127**, 244704 (2007).

[43] L. Triggiani, A. B. Muñoz-García, A. Agostiano, and M. Pavone, "Promoting oxygen vacancy formation and p-type conductivity in SrTiO₃ via alkali metal doping: A first principles study," Phys. Chem. Chem. Phys. **18**, 28951–28959 (2016).

[44] R. Pentcheva and W. E. Pickett, "Avoiding the polarization catastrophe in LaAlO₃ overlayers on SrTiO₃(001) through polar distortion," Phys. Rev. Lett. **102**, 107602 (2009).

[45] J. P. Perdew, A. Ruzsinszky, G. I. Csonka, O. A. Vydrov, G. E. Scuseria, L. A. Constantin, X. Zhou, and K. Burke, "Restoring the density-gradient expansion for exchange in solids and surfaces," Phys. Rev. Lett. **100**, 136406 (2008).

[46] A. H. Larsen, J. J. Mortensen, J. Blomqvist, I. E. Castelli, R. Christensen, M. Dułak, J. Friis, M. N. Groves, B. Hammer, C. Hargus, E. D. Hermes, P. C. Jennings, P. B. Jensen, J. Kermode, J. R. Kitchin, E. L. Kolsbjerg, J. Kubal, K. Kaasbjerg, S. Lysgaard, J. B. Maronsson, T. Maxson, T. Olsen, L. Pastewka, A. Peterson, C. Rostgaard, J. Schiøtz, O. Schütt, M. Strange, K. S. Thygesen, T. Vegge, L. Vilhelmsen, M. Walter, Z. Zeng, and K. W. Jacobsen, "The atomic simulation environment—A Python library for working with atoms," J. Phys.: Condens. Matter **29**, 273002 (2017).

[47] G. Pizzi, A. Cepellotti, R. Sabatini, N. Marzari, and B. Kozinsky, "AiiDA: Automated interactive infrastructure and database for computational science," Comput. Mater. Sci. **111**, 218–230 (2016).

[48] A. P. Bartók, R. Kondor, and G. Csányi, "On representing chemical environments," Phys. Rev. B **87**, 184115 (2013).

[49] A. P. Bartók, M. C. Payne, R. Kondor, and G. Csányi, "Gaussian approximation potentials: The accuracy of quantum mechanics, without the electrons," Phys. Rev. Lett. **104**, 136403 (2010).

[50] S. Cho, C. Yun, S. Tappertzhofen, A. Kursumovic, S. Lee, P. Lu, Q. Jia, M. Fan, J. Jian, H. Wang, S. Hofmann, and J. L. MacManus-Driscoll, "Self-assembled oxide films with tailored nanoscale ionic and electronic channels for controlled resistive switching," Nat. Commun. **7**, 12373 (2016).

[51] K. Tsuda and M. Tanaka, "Refinement of crystal structure parameters using convergent-beam electron diffraction: The low-temperature phase of SrTiO₃," Acta Crystallogr., Sect. A: Found. Crystallogr. **51**, 7–19 (1995).

[52] Y. A. Abramov, V. G. Tsirelson, V. E. Zavodnik, S. A. Ivanov, and I. D. Brown, "The chemical bond and atomic displacements in SrTiO₃ from X-ray diffraction analysis," Acta Crystallogr., Sect. B: Struct. Sci. **51**, 942–951 (1995).

[53] J. D. McCullough, "An X-ray study of the rare-earth oxide systems: Ceᴵⱽ—Ndᴵᴵᴵ, Crᴵⱽ—Prᴵᴵᴵ, Ceᴵⱽ—Prᴵⱽ and Prᴵⱽ—Ndᴵᴵᴵᴵ," J. Am. Chem. Soc. **72**, 1386–1390 (1950).

[54] B. Feng, I. Sugiyama, H. Hojo, H. Ohta, N. Shibata, and Y. Ikuhara, "Atomic structures and oxygen dynamics of CeO₂ grain boundaries," Sci. Rep. **6**, 20288 (2016).

[55] R. I. Eglitis and D. Vanderbilt, "First-principles calculations of atomic and electronic structure of SrTiO₃(001) and (011) surfaces," Phys. Rev. B **77**, 195408 (2008).

[56] J. Narayan and B. C. Larson, "Domain epitaxy: A unified paradigm for thin film growth," J. Appl. Phys. **93**, 278–285 (2002).

[57] P. P. Dholabhai, E. Martinez, N. T. Brown, and B. P. Uberuaga, "On the mobility of carriers at semi-coherent oxide heterointerfaces," Phys. Chem. Chem. Phys. **19**, 23122–23130 (2017).

[58] N. Schichtel, C. Korte, D. Hesse, and J. Janek, "Elastic strain at interfaces and its influence on ionic conductivity in nanoscaled solid electrolyte thin films—Theoretical considerations and experimental studies," Phys. Chem. Chem. Phys. **11**, 3043–3048 (2009).

[59] C. Korte, J. Keppner, A. Peters, N. Schichtel, H. Aydin, and J. Janek, "Coherency strain and its effect on ionic conductivity and diffusion in solid electrolytes—An improved model for nanocrystalline thin films and a review of experimental data," Phys. Chem. Chem. Phys. **16**, 24575–24591 (2014).

[60] J. A. Hirschfeld and H. Lustfeld, "First-principles study and modeling of strain-dependent ionic migration in ZrO₂," Phys. Rev. B **84**, 224308 (2011).

[61] S. Hull, "Superionics: Crystal structures and conduction processes," Rep. Prog. Phys. **67**, 1233 (2004).